Match reflection and formation of transient toroidal helium plasma

Kooij, V.L.; Bouwmeester, D.

Mach reflection and formation of transient toroidal helium plasma

Vincent L. Kooij [1,*] and Dirk Bouwmeester [1,2]
[1]*Huygens-Kamerlingh Onnes Laboratory, Leiden University, Leiden, The Netherlands*
[2]*Department of Physics, University of California, Santa Barbara, California 93106, USA*

(Received 25 March 2025; accepted 6 June 2025; published 25 November 2025)

Laser-generated, transient toroidal helium plasma at atmospheric pressure is studied experimentally. Tomographically reconstructed cross-sectional images reveal the gas flow responsible for the formation of the toroidal structure. A splitting of the toroidal plasma during the final phase of its evolution is observed. The plasma dynamics is induced by a two-lobed plasma kernel resulting from a single, focused laser pulse. This kernel generates two shocks that join to form an enhanced third shock, a so-called Mach reflection, in the plane perpendicular to the optical axis. This shock pattern determines the gas flow, which deforms the plasma into a disk, then transforms it into a nonrotating toroid, and finally splits it into two parallel rings. Schlieren imaging, a novel laser scanning-probe imaging technique, thermodynamic modeling, and a deliberately broken flow symmetry confirm this formation mechanism. This study is of interest for the generation of compact toroidal plasma structures in free space, with potential applications in chemical reactors, laser ignition of internal combustion engines, plasma medicine, and linked magnetic field line plasma confinement.

DOI: 10.1103/r96j-1lhd

I. INTRODUCTION

Toroidal plasma structures have been observed in a wide variety of experiments, including high-power electric arcs [1], high-speed microjets [2], nanosecond discharges [3], laser ignition of flammable mixtures [4–8], and laser-induced breakdown plasmas [9–11]. Potential applications and natural occurrences of free-space toroidal plasma structures are renewable energy storage [12], planetary nebulae [13], plasma medicine [14], industrial chemical reactors [15,16], and linked magnetic field line plasma confinement [17].

In magnetic confinement fusion—the leading approach for an economically viable nuclear fusion reactor—the topology of the plasma confining fields plays a pivotal role. The connection between stability and topology, established by Moffatt [18], has recently been confirmed by magnetohydrodynamics simulations, demonstrating that a magnetic field with helicity reconfigures itself into a structure of foliated toroidal surfaces [17]. These self-organizing knotted magnetic structures are intrinsically stable and essentially different from the tokamak—their hydrostatic pressure is minimal on the central circle of the foliated tori, and their magnetic pressure is balanced by the ambient hydrostatic pressure. Toroidal topological structures were used to construct an analytical solution of the equations of magnetohydrodynamics, which consists of a magnetic field configuration of closed magnetic field lines that are all linked to each other [19,20]. These structures were also used to investigate linked and knotted beams of light [21–24], gravitational radiation [25], and astrophysical environments [26].

The research presented in this paper was motivated by the multitude of concepts related to free-space toroidal plasma structures. A possible first step towards experimental studies, as presented in this paper, is to create a transient free-space toroidal plasma and understand its formation in detail. Subsequent steps could include microwave heating and flow control to sustain and manipulate the plasma. The toroidal structures presented in this paper are afterglow plasma resulting from a single laser-induced breakdown plasma, created in quiescent, atmospheric pressure helium gas at room temperature (see Sec. II). They are more symmetrical than those reported in the aforementioned experimental studies. Figure 1 presents an overview of the development of these toroidal plasma structures.

The origin of the toroidal structure and the splitting of the toroidal plasma during the final phase of its evolution are traced back to the structure of the two-lobed plasma kernel generated by the focused laser beam in the first 100 ns (see Sec. III). The shocks generated by this kernel are imaged using high-speed Schlieren imaging and a novel scanning-probe imaging technique that uses a second laser-induced breakdown plasma as a probe (see Sec. IV). These shocks join to form a third shock, a so-called Mach reflection, on a timescale of 100–500 ns (see Sec. V). It is this shock pattern and the associated low-pressure region that determines the gas flow. This flow deforms the plasma into a disk (at 5–10 μs), then transforms it into a nonrotating toroid (at approximately 20 μs), and finally splits it into two parallel rings (at 40–50 μs) (see Fig. 1 and Sec. VI).

Tomographically reconstructed cross-sectional images of the toroidal plasma (see Sec. VI A) visualize the gas flow

*Contact author: hello@vincentkooij.com; https://vincentkooij.com

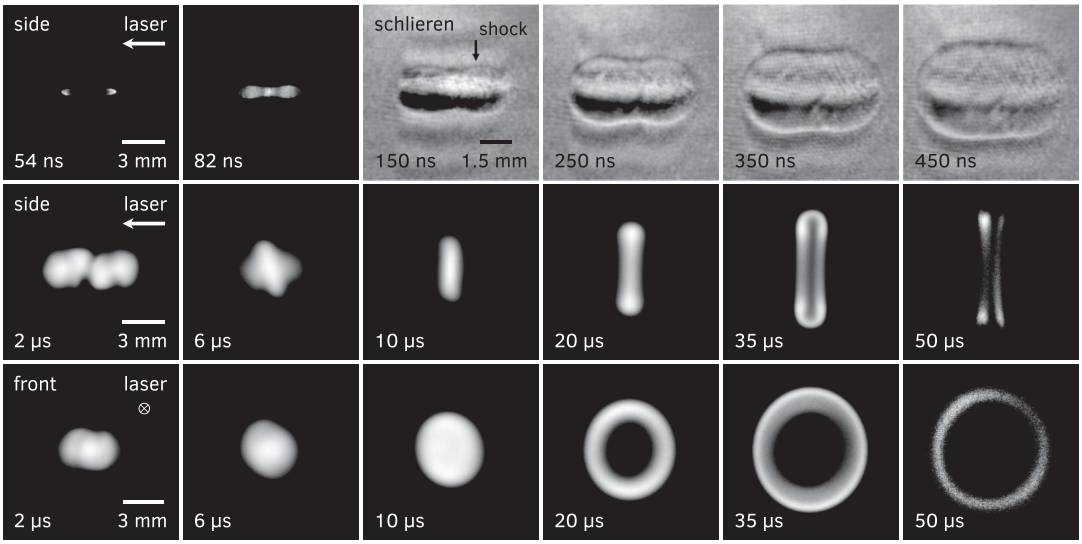

FIG. 1. Overview of the development of a toroidal plasma. (54–82 ns) Side view of the early development of a laser-induced breakdown plasma, showing the typical two-lobed plasma kernel. (150–450 ns) Side view Schlieren images visualizing the propagating shock generated by the plasma kernel. (2–50 µs) Side view (second row) and front view (third row) of the development of a toroidal plasma, from an evolved plasma kernel to the toroidal structure. The front views show slightly oval plasma structures due to a necessary skewed viewing direction. Side and front views are captured through a 10 nm bandpass filter enclosing the atomic helium emission lines at 587.6 nm and are individually normalized to their maximum intensity.

responsible for the generation of the toroidal structure (see Sec. VII). Thermodynamic modeling of the characteristic timescale involved in the generation of the toroidal plasma (see Sec. VIII) and a plasma flow experiment with a deliberately broken flow symmetry (see Sec. IX) confirm the formation mechanism. Section X presents our conclusions and a brief discussion on potential applications and further research based on the findings reported in this paper.

II. EXPERIMENTAL SETUP

A schematic of the high-power optical setup for generating and characterizing free-space toroidal plasma structures is shown in Fig. 2. Two Q-switched Nd:YAG lasers (Quanta-Ray GCR-3 and Continuum NY61-10) provide high-power laser pulses with a wavelength of 1064 nm, a temporal pulse length of approximately 10 ns, and a beam width of 8 mm. The pulse energy is adjustable between 0 and 300 mJ. In the plasma chamber, the laser pulses are focused into quiescent, atmospheric pressure, 5.0 grade helium gas, using a plano-convex lens with a focal length of 50 mm.

The experiments in Sec. IV present a novel scanning-probe imaging technique for imaging shocks and require successive laser pulses to be generated at intervals ranging from a few tens of nanoseconds to 100 microseconds. This is achieved by combining both laser beams using a polarizing beam splitter, after rotating the polarization of the laser pulses from the Continuum laser by 90° using a half-wave plate.

Before the laser pulses enter the plasma chamber, the combined beam path is split and recombined again, to displace and fine-tune the focus of the vertically polarized pulses in the plasma chamber relative to the focus of the horizontally polarized pulses.

To visualize shocks with a second laser-induced breakdown plasma as a scanning probe, the vertically polarized laser pulses are split off in the plasma chamber using a

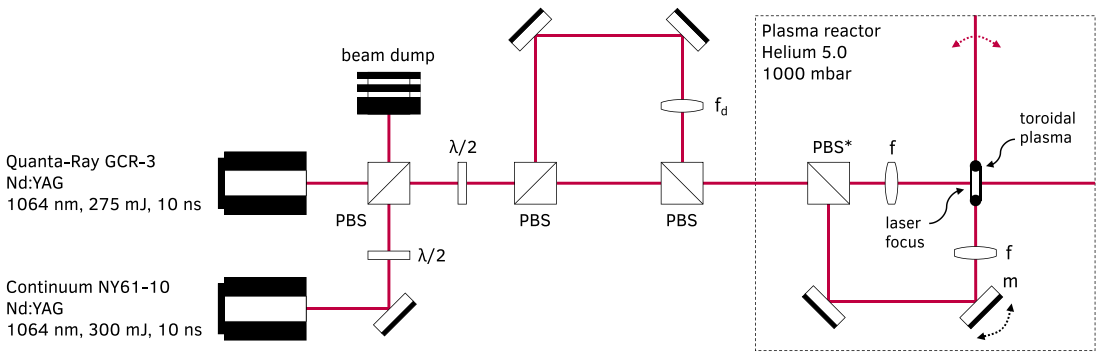

FIG. 2. Schematic of the high-power optical setup. PBS: polarizing beam splitter, PBS*: removable polarizing beam splitter, λ/2: half-wave plate, f: focusing lens, f_d: lens to displace the focus inside the plasma chamber, m: rotating mirror.

removable polarizing beam splitter. These pulses are then focused at a 90° angle with respect to the original beam path. This angle is adjustable using a piezoelectric inertia actuator, so that one laser can scan through a plasma created earlier using the other laser.

The Q-switch and flash lamp trigger signals for both lasers are generated by a digital delay generator and a FPGA (field-programmable gate array) pulse generator. The ICCD (intensified CCD) camera (Princeton Instruments PI-MAX 512) is triggered by the delay generator before the Q-switch is triggered, so that it is possible to image the onset of a laser-induced breakdown plasma.

The intensity of the plasma decreases orders of magnitude during its evolution from a laser-induced breakdown plasma to the final toroidal plasma. When studying the toroidal plasma, emission from the initial and very bright breakdown plasma can cause artifacts in the recorded images. Therefore, the Q-switches operate at a reduced repetition rate of 2.5 Hz while the flash lamps operate at the normal rate of 10 Hz. This minimizes unnecessary emission leaking through the MCP (microchannel plate) of the ICCD camera while attaining the maximum possible image capture rate.

The delay generator also triggers a 1 GHz bandwidth oscilloscope used for precise timing analysis and for recording the temporal profile of the laser pulse and plasma emission using a 150 ps rise time photo detector.

The imaging setup (not shown) consists of two achromatic 4f lens configurations capable of simultaneously imaging the side (orthogonal to the laser propagation direction) and front of the toroidal plasma by combining both views through a 50/50 nonpolarizing beam splitter.

The front view is necessarily skewed approximately 26° to avert blocking of the high-power laser beam by the imaging optics.

The images recorded by the ICCD camera are single shots. During an experiment, plasma is created repeatedly and each image is captured from a distinct plasma. Because the single-shot images are quite reproducible, most images presented in this paper are averaged over 50 repetitions to improve the signal-to-noise ratio.

The generated toroidal plasma structures are similar to commonly used laboratory helium plasmas, in the sense that they are optically thin (see, e.g., Refs. [27,28]) and exhibit a typical line spectrum; see, e.g., Refs. [27,29–32]. High-speed spectra, recorded using a prism spectrograph coupled to the imaging system of the ICCD camera, have shown that most emission originates from neutral atomic helium. In order to facilitate quantitative analyses, all images were therefore captured through a 10 nm bandpass filter with a center wavelength of 590 nm. This filter encloses the atomic helium emission lines at 587.6 nm, originating from the $1s3d\,^3D$-$1s2p\,^3P$ multiplet transitions [33]. To block out-of-band emission a 750 nm short-pass filter was used.

All images used for quantitative analyses are corrected for flat field, background emission, dark frame, and bias frame. A flat field correction is imperative as it shows variations of up to 15% and a honeycomb structure that distorts all recorded images. This is not unique to our camera; see, e.g., Ref. [34]. The background correction uses the edge columns of a recorded image as a reference, to simultaneously correct for both stray light and diffuse reflections from within the imaging system.

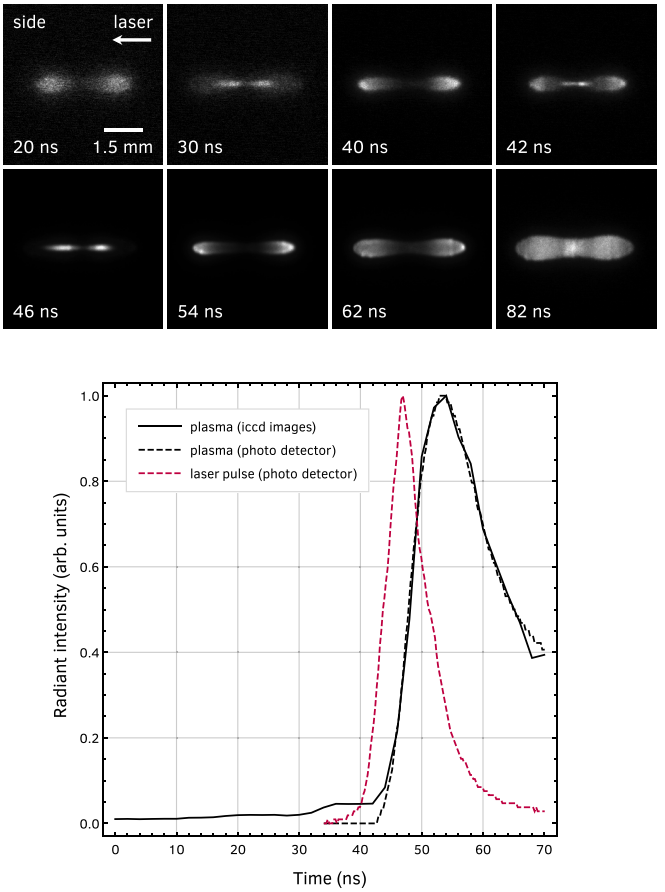

FIG. 3. (Images) Side view of the evolution of a laser-induced breakdown plasma. Note the repeated creation of plasma visible in the two-lobed plasma kernel. At 42 ns the main breakdown plasma is created, visible as a small and bright plasma within the preexisting plasma kernel. Images are individually normalized to their maximum intensity. Camera gate width: 2 ns, camera image averaging: none. (Graph) Intensity of the plasma kernel (dashed black line) and laser pulse (dashed purple line) obtained using a photo detector, along with the integrated intensity of the plasma images (solid black line). Traces are individually normalized to their maximum and averaged over 100 recordings. Note that $t = 0$ can be chosen arbitrarily.

The variable intensity of the plasma is attenuated using different neutral density filters rather than changing the gain or exposure time of the ICCD camera. This averts possible nonlinear behavior of the ICCD camera contaminating the quantitative measurements. Overlapping series were recorded and later glued together to produce a single set of images spanning the entire evolution of the plasma. The least intense series were recorded without a neutral density filter, hence sets obtained with different laser pulse energies can be compared.

III. PLASMA KERNEL DYNAMICS

The two-lobed plasma kernel that generates the toroidal helium plasma is shown in Fig. 3. This plasma was created by individual laser pulses with an energy of 275 mJ. The images were recorded with an exposure time of 2 ns and without

a bandpass filter. The same figure presents their integrated intensity (solid black line) as well as intensity measurements of the plasma kernel and laser pulse (respectively black and purple dashed lines) separately obtained using a photo detector with respectively a 750 nm short-pass filter and a 1000 nm long-pass filter. The measurements were synchronized by correlating the plasma intensity traces and shifting the photo detector traces in the time domain.

Surprisingly, tens of nanoseconds before the bright plasma pulse is observed, repeated creation of faint plasma is visible. Some 30 ns before the main laser pulse, a small and faint two-lobed plasma is discernible. This plasma slightly expands for 20 ns, after which a second, smaller but brighter, two-lobed plasma is created within the preexisting plasma kernel. This plasma likewise expands for 12 ns, after which, once again, an even smaller but still brighter, two-lobed plasma is created at 42 ns, marking the beginning of the main laser pulse. Tens of nanoseconds later, the two-lobed plasma fills up and emission is observed from the entire elongated plasma. Note the 4 ns delay between the main laser pulse and the bright plasma pulse.

The repeated creation of plasma can be attributed to the formation of the giant pulse in the Q-switched Nd:YAG laser. Initially, the photon density is small, but then grows exponentially leading to the formation of the giant pulse [35]. During the exponential growth, the photon density is small compared to the giant pulse, but it can nevertheless be sufficient to induce breakdown and create a faint plasma. The photo detector did not observe this weak emission, probably because its optics were aligned to optimally image the bright central spot.

In general, a laser-induced breakdown plasma is created as a result of avalanche ionization, where multiphoton ionization provides the initial seed electrons necessary to ignite the avalanche [36]. Subsequent inverse bremsstrahlung absorption heats the plasma [37], creating a high-pressure and high-temperature plasma kernel whose rapid expansion leads to the formation of a shock [10,38–40].

The repeated creation of plasma in the plasma kernel may contribute to the formation of its two-lobed structure by successively creating small, low-density cavities, thereby increasing the breakdown threshold and inhibiting the creation of additional plasma in the center.

The plasma kernels presented in Fig. 3 strikingly resemble the kernels recently reported in studies on the onset and dynamics of plasma kernels in atmospheric air [41,42]. The reported nonequilibrium three-temperature plasma model is in good agreement with experimental observations and accounts for multiphoton ionization, inverse bremsstrahlung absorption, chemical kinetics, shock dynamics, and radiation propagation. Different mechanisms have been identified, including self-focusing, lens aberration, and hydrodynamic instabilities [43], but the importance of each contribution is not yet fully understood [42].

Despite addressing laser-induced breakdown in air, which requires a chemical kinetics component accounting for the plasma chemistry of the constituents of air, the dynamics of this model is very similar to that of the plasma kernels presented in this paper. This resemblance confirms the broader applicability of the three-temperature plasma model.

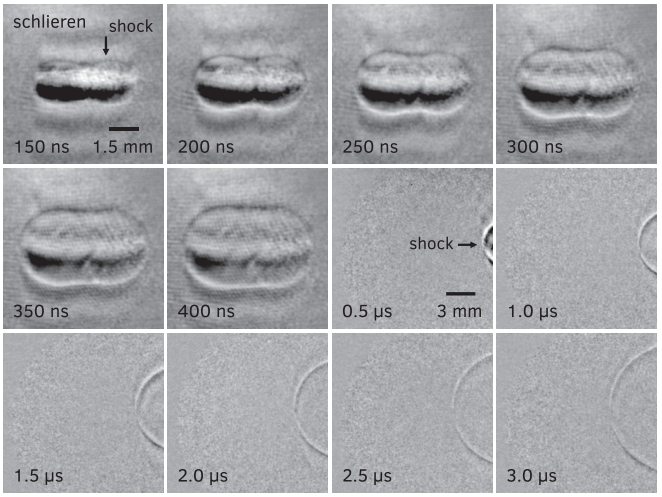

FIG. 4. Side view Schlieren images visualizing the propagating shock generated by a laser-induced breakdown plasma. Images are corrected for plasma emission still visible through the Schlieren imaging system. In the bottom row, the breakdown plasma is moved out of sight, to the right of the image. Laser pulse energy: 275 mJ, camera gate width: 2 ns, camera image averaging: 10.

IV. SHOCKS AND SUCCESSIVE LASER PULSE EXPERIMENTS

Inverse bremsstrahlung absorption during the main laser pulse heats the plasma [37], creating a high-pressure and high-temperature plasma kernel whose rapid expansion leads to the formation of a shock [10,38–40]. The propagation of this shock, and the expanding low-density region created in its wake, are visualized in Fig. 4 using high-speed Schlieren imaging with a helium-neon laser source. This technique is sensitive to the first derivative of the density, in the direction normal to a knife edge positioned in the shared focal plane of the 4f lens system used for imaging the side of the toroidal plasma [44]. A 4 mW collimated 632.8 nm helium-neon laser beam was used together with a laser line filter (Thorlabs FL632.8-10) to block most plasma emission. In the bottom row, the breakdown plasma is moved out of sight, to the right of the image, to be able to image the shock at later times.

Due to the brightness of the plasma, the plasma emission still visible through the helium-neon laser line filter interferes with the helium-neon laser used for Schlieren imaging. The Schlieren images are corrected for this by subtracting images that were captured while the helium-neon laser was switched off. Small variations in plasma creation—recall that plasma is created repeatedly and each image is captured from a distinct plasma (see Sec. II)—limit the effectiveness of this correction and are the most probably cause of the features seen between the central part of the plasma and the shock boundary.

Complementary to Schlieren imaging, a novel technique was used to visualize the propagation of the shock, wherein a second laser-induced breakdown plasma is used as a scanning probe. At the time of interest, and delayed with respect to the main breakdown laser pulse, a second breakdown plasma was created by a second high-power Nd:YAG laser. The creation and subsequent evolution of this plasma is highly sensitive to

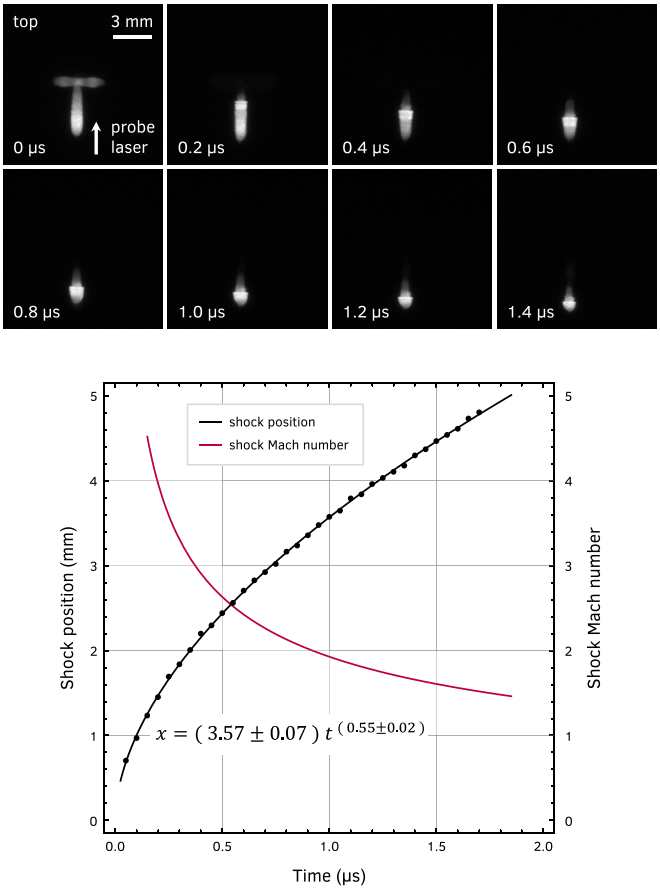

FIG. 5. (Images) Top view of the propagating shock generated by a laser-induced breakdown plasma, visualized using a second laser-induced breakdown plasma as a probe. The shock manifests itself as the sharp and clear edge visible in the second breakdown plasma. At 0 µs both the main and second breakdown plasma are visible. (Graph) Shock position and shock Mach number derived from the top view images. The shock position (black dots) is fitted against a power-law function (black line) and the shock Mach number (purple line) is obtained by differentiation of the fitted shock position. The speed of sound is approximately 1020 m/s.

the local density, which is dictated by the main breakdown plasma, and is even completely suppressed in regions of low density. Laser probe techniques are very common in many fields of research, such as NMR (nuclear magnetic resonance) and AMO (atomic, molecular, and optical) physics, but to the authors' knowledge visualizing the propagation and cross section of shocks with a laser-induced breakdown plasma as a scanning probe is novel. Somewhat related works concern plasma dynamics in gas-filled hollow-core photonic crystal fibers [45] and double-pulse laser-induced breakdown spectroscopy [46].

Figure 5 shows the top view of the propagating shock obtained using this technique, where at zero delay both the main and second breakdown plasma are visible. By increasing the delay, the propagating shock—manifesting itself as the sharp and clear edge visible in the second breakdown plasma—moves through the images.

The second breakdown plasma was created at a distance from the main breakdown plasma. If this plasma had been created at the same position as the main plasma, it would be completely suppressed for a range of delays. This suppression is also observed in the density measurements presented in Sec. VIII B and is likewise reported in the literature [6,11].

The likelihood that the creation of the second plasma results in modified propagation of the shock generated by the main breakdown plasma is minimal. Recall that plasma is created repeatedly and that every recorded image is captured from a distinct plasma (see Sec. II). Moreover, the time span for creating this plasma is approximately 40 ns (see Fig. 3). This means that for each image in Fig. 5, the shock generated by the main plasma is propagating freely until the second plasma is created, and from the same figure it is clear that in the 40 ns of creating this plasma, the propagation of the shock is minimal. Also note that the camera gate width of these images is only 2 ns.

The shock generated by a laser-induced breakdown plasma resembles the blast wave generated by a nuclear explosion [47–49] and is also observed in supernova remnants [50,51]. Basic blast wave theory was independently proposed by Taylor [47], Von Neumann [49], and Sedov [52] and assumes an instantaneous energy release into an infinitesimally small volume. Following the energy release, the motion of the shock is described by a power-law time dependence, which for spherical symmetry has a 0.4 exponent [47,52,53].

In Fig. 5 the position of the shock is presented together with its shock Mach number. The position of the shock is fitted against a power law and shows that the shock propagates with an exponent of 0.55 ± 0.02.

The discrepancy with blast wave theory can be explained from the observation that our plasma kernel exhibits a two-lobed structure, which rudimentary can be seen as a two-dimensional explosion, where a $t^{0.5}$ dependence is expected [52]. Moreover, blast wave theory assumes an instantaneous energy release and neglects internal heat transfer phenomena, including radiation and ionization, both of which require more sophisticated models [54]. Earlier studies reported a time dependence of $t^{0.6}$ during the interval between breakdown and the end of the laser pulse [5] and a t^1 dependence can be observed during the free expansion phase of a supernova remnant [50]. If the $t^{0.55}$ dependence is interpreted as the signature of a driven and reinforced shock, the relaxation of metastable helium atoms might be the source of the driving energy.

The shock Mach number presented in Fig. 5 is obtained by differentiation of the fitted shock position. During the early expansion, speeds of up to Mach 4 are observed. The speed of sound in this experiment is approximately 1020 m/s. When the shock Mach number approaches one, this marks the end of the shock expansion and the shock proceeds at sonic speeds [53]. For the shock presented in Fig. 5 this occurs at 4.3 µs, which qualitatively matches the characteristic timescale of 6.7 µs found using the thermodynamic model presented in Sec. VIII.

Similar to the method used to visualize the propagating shock, the entire shock can be visualized by sweeping the second breakdown plasma through the low-density region at a fixed delay. In Fig. 6 these measurements are presented for a delay of 1 µs. By combining all individually captured images, a representative image of the shock is obtained. Note that only

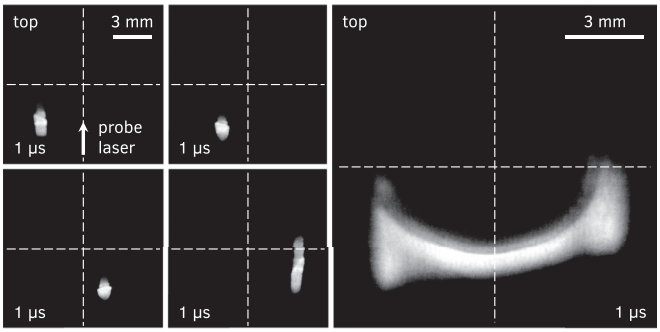

FIG. 6. Cross section of the shock generated by a laser-induced breakdown plasma, visualized using a second laser-induced breakdown plasma as a scanning probe. (Left quartet) Top view images captured 1 µs after the main breakdown laser pulse, while sweeping the second breakdown plasma through the shock. (Right) The entire shock, visualized by combining all top view images.

half of the low-density region is visible because of the limited extent of the breakdown plasma created by the second laser.

To correlate the two techniques used above, images of the probing breakdown plasma are combined with Schlieren images of the shock generated by the main breakdown plasma created earlier. Comparing the two leftmost images in Fig. 7, obtained respectively with and without the main breakdown plasma present, it is clear that the probing breakdown plasma is expelled outward. The combined plasma and Schlieren image shows that the probing plasma is expelled outward, exactly to the point where the shock separates the low-density region from the ambient gas.

V. MACH REFLECTION AND LASER-INDUCED BREAKDOWN PLASMA

Reviewing the plasma kernel images in Fig. 3 shows that at 54 ns the plasma emission is at its brightest. Precisely at this moment, the plasma kernel exhibits a two-lobed structure consisting of two, almost isolated, bright plasmas. Both high-pressure and high-temperature plasmas expand rapidly, leading to the formation of two shocks. The imprint of these shocks was already visible in the Schlieren images presented in Fig. 4, most notably around 250 ns, where two overlapping spherical shocks are clearly visible.

This Schlieren image is reproduced in Fig. 8. In the region of the two overlapping shocks, a so-called Mach reflection is

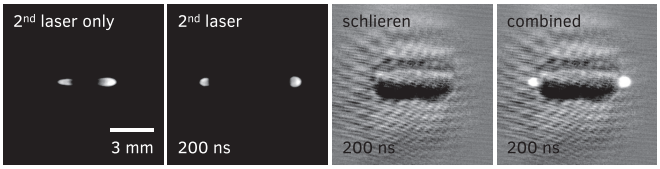

FIG. 7. Combined plasma and Schlieren images (combined) show that a second, probing, laser-induced breakdown plasma (second laser) is created on the edge of the shock (schlieren) generated by a preceding laser-induced breakdown plasma (not shown). Without the preceding plasma, the probing plasma shows its regular two-lobed structure (second laser only).

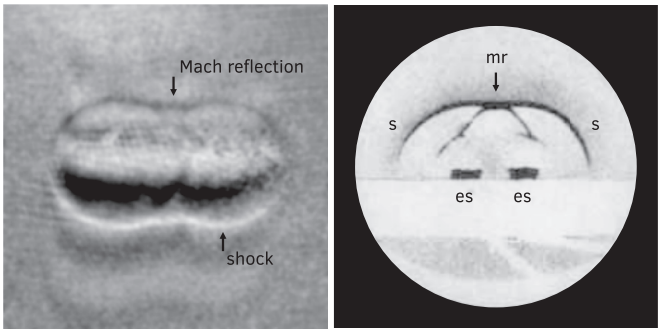

FIG. 8. Mach reflection of shocks generated by the two-lobed plasma kernel of a laser-induced breakdown plasma. (Left, reproduced from Fig. 4 at 250 ns) Schlieren image of the shocks generated by the two-lobed plasma kernel. (Right) First visualization of the interaction of shocks by Ernst Mach. Two spherical shocks (s) are generated by two electric sparks (es) near a glass plate. The interacting shocks generate a third shock known as a Mach reflection (mr). Reproduced from Ref. [57] with permission of Wiley-VCH GmbH.

discernible. A sufficiently oblique interaction of two shocks generates a new shock, which has a higher strength and propagates faster than the primary shocks [55]. The two shocks join to form a third shock, the Mach reflection. Because the Mach reflection significantly increases the strength of the shock, it was studied by Reines and Von Neumann to determine the optimum height of burst of an atomic bomb, to provide the greatest possible destructive effect on the ground [55,56].

In Fig. 8, alongside the Schlieren image of the two interacting shocks, a historical image by Mach *et al.* [57,58] is reproduced and the resemblance is striking. In this historical image, Mach visualized the interaction of two almost spherical shocks generated using two electric sparks.

Numerical studies on the onset and dynamics of plasma kernels [38,41,42] report plasma structures that are strikingly similar to our Schlieren image, and thus to the shock interaction as presented by Mach *et al*. These studies also show that a Mach reflection indeed represents a stronger and more dense shock, as the authors noted [38], but they did not identify it as a Mach reflection. In a laser-induced breakdown spectroscopy study [54] the reflection of a shock on a brass surface was indeed identified as a Mach reflection.

The fact that a Mach reflection represents a stronger shock explains the asymmetric gas flow necessary for the generation of a toroidal plasma. The higher intensity of the Mach reflection breaks the symmetry. Consequently, the replenishing gas flow orthogonal to the symmetry axis commences later.

VI. TOROIDAL PLASMA DEVELOPMENT AND TOMOGRAPHIC RECONSTRUCTION

The toroidal plasma structures presented in this paper emerge solely as a result of a single laser-induced breakdown plasma, created in quiescent, atmospheric pressure, helium gas at room temperature. In Figs. 9 and 10 the evolution of

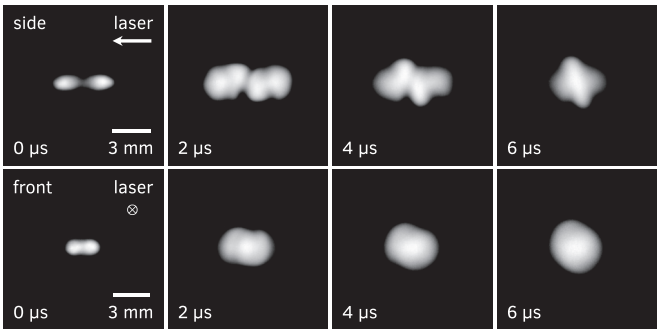

FIG. 9. Side and front view of the development of a toroidal plasma. Shown is the first part of the evolution, from an evolved plasma kernel to a plasma pillbox. This sequence is continued in Fig. 10. The front views show slightly oval plasma structures due to a necessary skewed viewing direction. Images are individually normalized to their maximum intensity. Camera gate width: 250 ns, camera image averaging: 50.

a breakdown plasma for a laser pulse energy of 250 mJ is presented, showing the emergence of the toroidal plasma and its splitting and subsequent dissolvement. Due to a necessary skewed viewing direction, the front views show slightly oval plasma structures. All images are recorded using a fixed gate width of 250 ns and a fixed gain of 255, and are individually normalized to their maximum intensity to respect the large dynamic range in intensity of the evolution.

The images recorded by the ICCD camera are captured from independent breakdown events. The gradual development of the presented images shows that the plasma evolution is very reproducible, warranting the averaging of the recorded images. The generation of the toroidal structure is attributable to gas flow along the symmetry axis of the plasma. This gas flow replenishes the low-density region created in the wake of the shock generated by the breakdown plasma. The earlier presented Schlieren images already visualized this shock and its associated low-density region.

A. Tomographic reconstruction

A visualization of the said gas flow is insightful but requires a three-dimensional tomographic reconstruction of the toroidal plasma. Such a reconstruction is feasible because the toroidal plasma is axially symmetric and optically thin. This means that the recorded images are two-dimensional projections of the three-dimensional toroidal plasma. Moreover, the side views, recorded orthogonal to the symmetry axis of the toroidal plasma, are in fact a projection of an axially symmetric object. This provides the necessary condition to employ Abel inversion [28] and tomographically reconstruct the toroidal plasma.

The middle row of Fig. 10 presents, in addition to the side and front views, cross-sectional images of the toroidal plasma obtained through a tomographic reconstruction, by means of Abel inversion of the individual columns of the recorded side view images.

The direct inversion of the Abel transform involves a derivative of the recorded image and is therefore rather sensitive to experimental noise [29,59,60]. A simple numerical Abel inversion using transform techniques based on the projection slice theorem [61] was conceived to mitigate this problem. Comparing the reconstructed and side view images illustrates the need to perform a tomographic reconstruction. Subtle features that are otherwise imperceptible become apparent.

The symmetry axis is highly sensitive to noise arising from a nearly singular condition in the reconstruction. This can be understood from the fact that the contribution from annuli near the symmetry axis is small compared to the contribution from larger distances [59,62]. This results in an accumulation of noise near the symmetry axis. To suppress artifacts that may arise, the one-pixel-wide symmetry axis is blackened in the reconstructed images. This is most apparent at 10 µs.

Since the Abel inversion must be applied to an even sequence, the side view images were symmetrized by discarding their top half. The inversion was then applied to the individual columns of the remaining bottom half of the image. This geometrically motivated symmetrization can be refined by calculating the position of the symmetry axis [63].

B. Toroid formation

In Figs. 9 and 10 a toroidal plasma is clearly visible from 20 µs onward. Previous laser-induced breakdown studies reported similar structures, most notably in nitrogen and air [9–11]. Likewise, studies on laser ignition of flammable alkane-air mixtures reported the emergence of toroidal flame kernels [4–6].

The plasma torus visible at 20 µs evolves into an eroded toroid prior to splitting into two halves. This new observation is a strong indication that, although the emerged plasma structure is of toroidal nature, it does not exhibit vorticity like the well-known vortex rings [64] or the structures reported in Refs. [4,5,9,10].

An explanation for this splitting is the symmetry of the breakdown plasma. Figure 9 shows that the laser-induced breakdown plasma at 0 µs exhibits a two-lobed structure which is highly symmetrical with respect to the focal plane. Numerical studies on the fluid dynamical effects of laser energy deposition show that the generation of vorticity stems from an asymmetrical, tear-drop-shaped, breakdown plasma [40,65]. This suggests that a highly symmetrical breakdown plasma inhibits the generation of vorticity in a toroidal plasma.

Figures 9 and 10 show features in common with earlier reported breakdown studies [9–11]. Summarized, these are the following:

0 µs: A laser-induced breakdown plasma is created due to the avalanche ionization of helium gas. Multiphoton ionization provides the initial seed electrons necessary to ignite the avalanche [36]. Subsequent inverse bremsstrahlung absorption heats the plasma [37], creating a high-pressure and high-temperature plasma kernel whose rapid expansion leads to the formation of a shock [10,39,40].

1 µs: The plasma kernel continues to expand, while the shock detaches from the kernel and propagates into the quiescent ambient gas, creating a low-density region in its wake. This shock, not visible here, is visualized using high-speed Schlieren imaging (see Sec. IV).

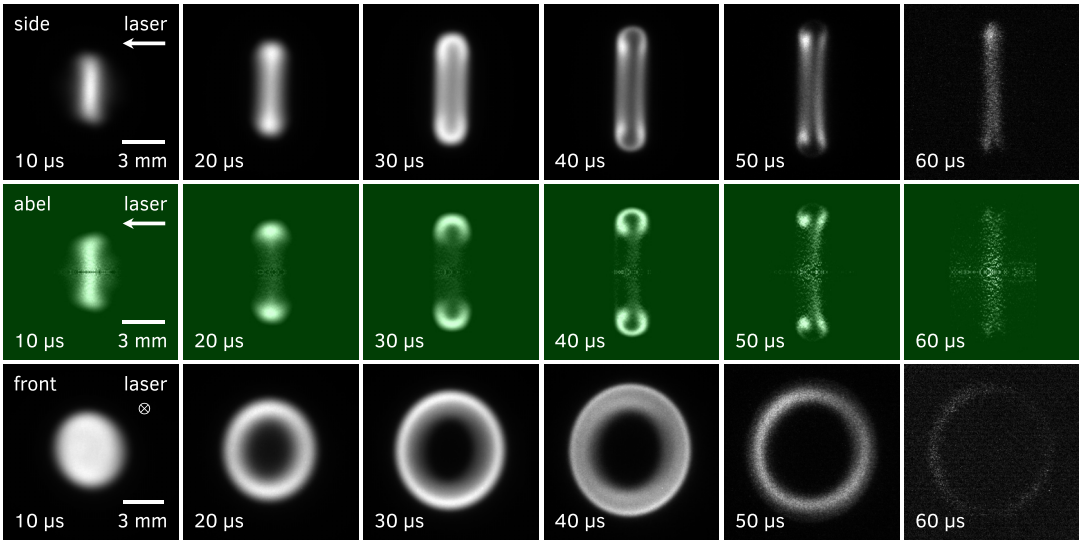

FIG. 10. Development, splitting, and subsequent dissolvement of a toroidal plasma. Shown is the second part of the evolution, from a plasma pillbox to the toroidal structure. Side and front view are a continuation of Fig. 9. The middle row shows cross-sectional images, obtained through a three-dimensional tomographic reconstruction of the side view images. The front views show slightly oval plasma structures due to a necessary skewed viewing direction. Images are individually normalized to their maximum intensity.

2–8 µs: The plasma is squeezed in the longitudinal direction due to gas flowing back to the plasma kernel along the symmetry axis, while it continues to expand transversely.

10 µs: A plasma pillbox forms as a result of the longitudinal compression and the evolution enters a more quiescent phase.

20 µs: A plasma torus has formed. The replenishing gas flow along the symmetry axis squeezed a hole into the plasma pillbox. The plasma torus is approximately 6.5 mm in diameter and 2 mm thick for a laser pulse energy of 250 mJ.

30–40 µs: Due to the symmetry of the breakdown plasma, the squeezing gas flow approaches the plasma from both sides with equal strength. These flows collide in the center of the torus and expand into a plane orthogonal to the symmetry axis, pushing the plasma outward. The plasma torus evolves into a deformed and eroded toroidal plasma.

50 µs: The flow deforming and eroding the toroidal plasma continues and dissects the toroidal plasma into two halves.

60 µs: The toroidal plasma dissolves and is no longer visible. This does not necessarily mean that a quiescent state is reached; gas flow may still be present.

The evolution outlined obviously depends on the specifics of the experiment. In this paper, after 20 µs, a plasma torus has formed. In Ref. [10], for example, where toroidal structures of similar size in air are studied, this occurs after 50 µs.

To correlate both observations, recall that the speed of sound in a gas is of the same order of magnitude as the mean speed of its constituents [66]. It is therefore tenable that it dictates how fast density variations equilibrate. The speed of sound in helium is about 3 times higher than in air, which supports the observations.

C. Different laser pulse energies and spectral radiant intensity

The evolution presented in Figs. 9 and 10 is exemplary and is likewise observed for laser pulse energies of 50, 100, and 200 mJ. Indeed, Fig. 11 presents images showing that the generation of the toroidal structure is robust over a wide range of pulse energies. In addition, it includes a graph of the evolution of the spectral radiant intensity.

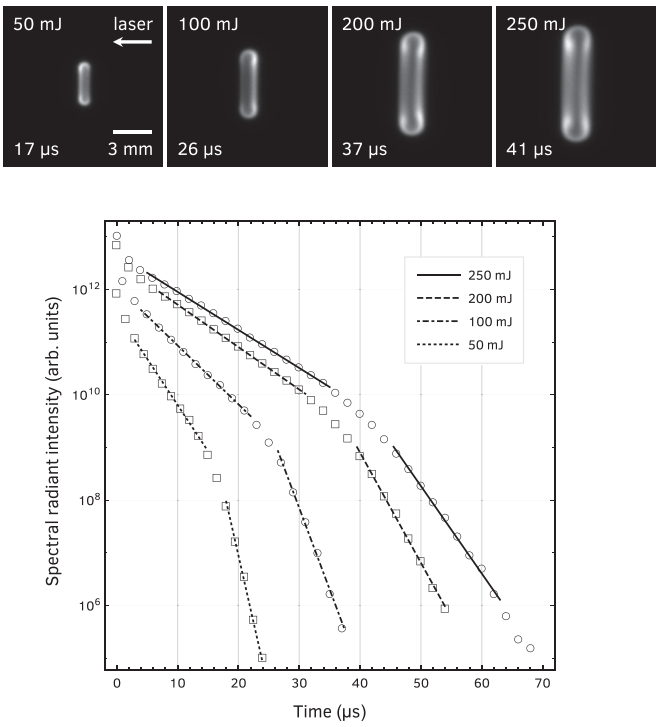

FIG. 11. (Graph) Spectral radiant intensity of a laser-induced breakdown plasma, shown for different laser pulse energies. Measurements are recorded at a 500 ns interval, but for clarity fewer are shown (markers). Each intensity graph shows two sections of exponential decay, both fitted to an exponential (line segments). (Images) Side views for the different laser pulse energies, recorded at the intersection of the extrapolated exponential line segments. Images are individually normalized to their maximum intensity.

Each intensity graph shows two sections of exponential decay, both fitted to an exponential. The similar morphology of the images recorded at the intersection of the extrapolated exponential line segments shows that this intersection is a key moment in the evolution of a toroidal plasma.

These kinks in the intensity graphs—signifying the beginning of a faster decay—result from gas flowing back into the low-density region, which increases the density around the plasma. Section VIII B will address this in more detail.

Given that the intensity mainly decays exponentially, while taking into consideration the massive change in plasma size and morphology during this decay, points to local plasma chemistry. Indeed, a zero-dimensional kinetic model of a pure helium plasma is shown to exhibit exponential decay of the electron density [67]. Furthermore, oxygen impurities contaminating the plasma chamber due to the desorption of air from the chamber walls, expresses itself in a similar way as a result of the attachment of electrons to oxygen molecules [36,68].

Ambipolar diffusion and recombination cannot account for the observed behavior, as these effects would, in this case, result in nonexponential decay. However, the above is based on a simplified model of what is in fact a complex dynamical process and might need modification.

VII. GAS FLOW VISUALIZATION

The gas flow responsible for the generation of the toroidal structure can be inferred from the motion of the plasma emission in the tomographically reconstructed cross-sectional images. To better visualize the core of the toroidal plasma, and hence the motion of the plasma emission, Fig. 12 presents false color cross-sectional images with smaller time increments than the images presented in Fig. 10.

The longitudinal compression forming the plasma pillbox mentioned in Sec. VI B, continues along the symmetry axis represented by the horizontal dashed line. At 16 μs, the squeezing gas flow, which replenishes the aforementioned low-density region, completely pinches off the center of the plasma pillbox, thereby generating a toroidal plasma.

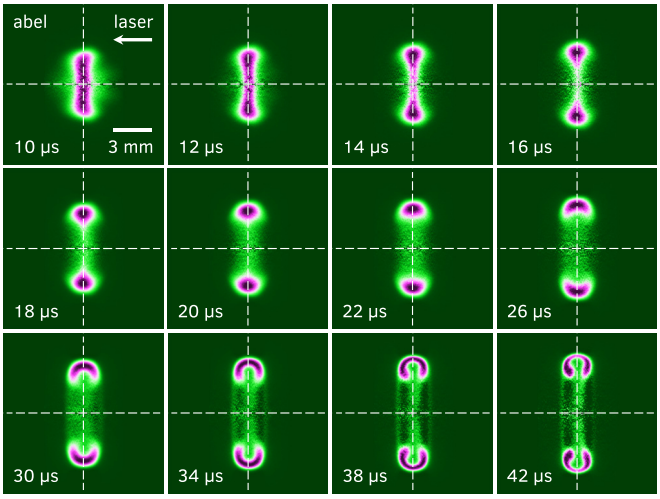

FIG. 12. False color cross-sectional images showing the development and subsequent deformation of the toroidal structure. The gas flow can be inferred from the motion of the plasma emission. The images are obtained through a three-dimensional tomographic reconstruction and clearly visualize the plasma core (purple and black). Images are individually normalized to their maximum intensity.

The two-lobed structure of the breakdown plasma is highly symmetrical with respect to the focal plane. As a result, the squeezing gas flow that approaches the plasma from both sides is approximately of equal strength. These flows collide in the center of the toroidal plasma and spread out into the symmetry plane orthogonal to the symmetry axis. This pushes the plasma outward and further deforms and erodes the toroidal plasma. The gas flow manifests itself more clearly from 26 μs onward as a horseshoe-shaped plasma in the cross-sectional images.

A flow speed is easily obtained. Considering the flow in the symmetry plane, in the images between 26 μs and 42 μs, results in a flow speed of 95 ± 3 m/s. Meanwhile, for a gas, the mean thermal speed of its constituents is given by

$$v = \sqrt{\frac{8}{\pi}\frac{kT}{m}} \tag{1}$$

where m is their mass, T the (ambient) gas temperature, and k the Boltzmann constant [66]. For helium at a temperature of 300 K the mean thermal speed is 1260 m/s [69]. Hence, the observed flow speed is roughly one-tenth of the mean thermal speed.

Since the toroidal plasma, by then, is fairly developed, the density in its center is partially restored by the replenishing gas flow. Therefore, the flow does not expand into vacuum, but into a region with a density of approximately 0.7 n_0 (see Sec. VIII B). The reduced flow speed therefore seems reasonable. At earlier times, the gas flow is not visible, but its speed will of course be higher.

VIII. CHARACTERISTIC TIMESCALE

The flow speeds involved in the generation of the toroidal structure are akin to the mean thermal speed of the helium atoms. A simple thermodynamic model offers a characteristic timescale at which structure is expected to develop. In all simplicity, it will not explain the mechanisms responsible for the generation of the toroidal structure. The origin of the necessarily asymmetric gas flow is addressed in Sec. V.

A. Characteristic timescale

To model the evolution of a low-density region, created in the wake of a shock generated by a laser-induced breakdown plasma, assume that the volume of this plasma is infinitesimally small, the work done on the gas is spherically symmetric in nature, and the laser pulse energy as a whole is converted into kinetic energy of the gas surrounding the plasma. For energies well above breakdown threshold this is fair because over 85% is absorbed by the plasma [10,39].

The low-density region will promptly increase in size until all kinetic energy of the gas is converted into potential energy of this region. The gas is now motionless. Assuming that the successive replenishment of the low-density region is dictated by the thermal motion of the constituents of the gas, a characteristic timescale is found by dividing the extremum

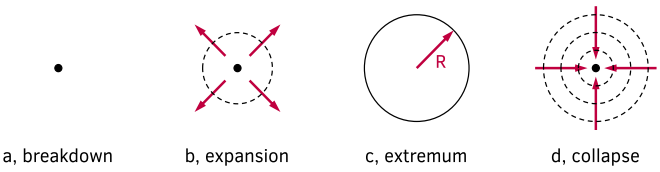

FIG. 13. Schematic of the evolution of a low-density region generated by an infinitesimally small, spherically symmetric laser-induced breakdown plasma. The evolution of this region is differentiated into four phases: breakdown, expansion, extremal radius, and collapse.

of the radius of this region by the mean thermal speed of the said constituents. Figure 13 illustrates this schematically. Naturally, more rigorous models exist [70–72].

Let E be the laser pulse energy, p the pressure of the ambient gas, and R the extremum of the radius of the low-density region. The work $p\,\mathrm{d}V$ done on the gas was assumed to be spherically symmetric in nature, therefore

$$E = \int p\,\mathrm{d}V = \frac{4}{3}\pi R^3\, p.$$

Let τ be the characteristic timescale defined as the time between breakdown and the collapse of the low-density region, and assume that the expansion and replenishment are of equal duration. Then

$$\tau = 2\,\frac{R}{v}$$

where v is the mean thermal speed given by Eq. (1).

Recognize that for an ideal gas, the equation of state is $p/\rho = kT/m$, where T is the (ambient) gas temperature, and ρ its mass density [73]. Even so, the characteristic timescale τ is more intelligibly written as

$$\tau = 2\sqrt{\frac{\pi}{8}\,\frac{m}{kT}}\left(\frac{3}{4\pi}\,\frac{E}{p}\right)^{\frac{1}{3}}.$$

For standard pressure helium at a temperature of 300 K and a pulse energy of 250 mJ, the characteristic timescale is 13.4 µs. This tallies fairly well with the images in Fig. 12, where the replenishing gas flow collides in the center of the toroidal plasma at 16 µs.

The calculated value is lower than observed experimentally because, as explained in Sec. VII, the observed flow speed is lower than the mean thermal speed. Yet the difference is smaller because this value is obtained at an earlier moment in the evolution, when the density, to a large extent, is still depleted.

B. Density of helium atoms in the center of the toroidal plasma

The calculated characteristic timescale is confirmed by a measurement of the evolution of the number density in the center of the toroidal plasma. A second laser-induced breakdown plasma is used as a probe. The intensity of this plasma is then used as a measure of the local number density, through correlation with calibration measurements obtained in quiescent helium gas at known densities. Figure 14 presents selected images illustrating this technique along with the inferred evolution of the density.

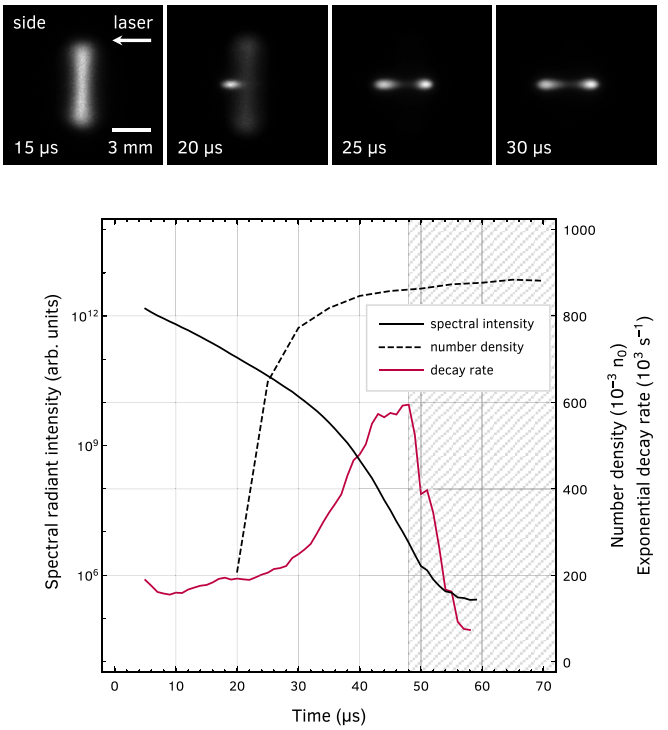

FIG. 14. (Graph) Number density in the center of the toroidal plasma (dashed line) measured using a second laser-induced breakdown plasma as a probe. The region where measurement noise becomes prominent is indicated by gray shading. The exponential decay rate (purple line) and the spectral radiant intensity (black line) are related to the toroidal plasma itself. Loschmidt constant $n_0 = 2.65 \times 10^{25}$ m^{-3}. (Figures) Side view of the probing plasma. (15 µs) Toroidal plasma and indiscernible (suppressed) probing plasma. (20 µs) Visible probing plasma and faintly visible toroidal plasma. (25 and 30 µs) Clearly visible probing plasma, toroidal plasma too faint to discern. Images are individually normalized to their maximum intensity.

It is evident that 20 µs after the breakdown laser pulse, the density in the center of the toroidal plasma is increasing rapidly. This is consistent with the timescale calculated in the previous subsection. It is unfortunate that the measurements obtained at earlier times are not trustworthy, for the reason that the intensity of the bright plasma pillbox itself prevents a sensible quantification of the intensity of the probing plasma.

For the toroidal plasma, Fig. 14 also shows the evolution of the spectral radiant intensity and its decay rate. The kink in the intensity graph—signifying the beginning of a faster decay—can be explained by the evolution of the density in the center of the toroidal plasma. This kink was identified earlier in Sec. VI C.

The decay rate starts to increase rapidly around 30 µs. This is roughly 10 µs later than the rapid increase of the density in the center of the toroidal plasma. Note that the region where measurement noise becomes prominent—signified by a decrease in the decay rate—is indicated by gray shading.

The delay is a consequence of the fact that the density measurements are performed in the center of the toroidal plasma, whereas the decay rate is derived from the intensity of the toroidal plasma, which is measured at a considerable distance from its center. In the cross-sectional images shown in Fig. 12

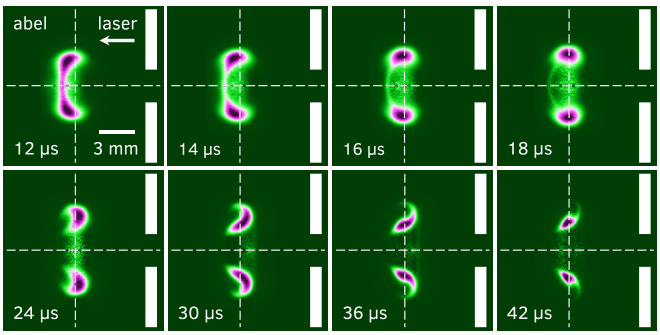

FIG. 15. False color cross-sectional images showing the development of a distorted toroidal structure as a result of a nearby, symmetry breaking, metal plate (two white rectangles, shown to scale). The metal plate has a 2.8 mm hole through which the laser pulses pass freely. The images are obtained through a three-dimensional tomographic reconstruction and clearly visualize the plasma core (purple and black). Images are individually normalized to their maximum intensity.

this is confirmed—the toroidal plasma evidently starts its deformation into a horseshoe-shaped plasma precisely when the decay rate starts to increase as a consequence of the arrival of the replenishing gas flow.

IX. PLASMA FLOW EXPERIMENT WITH A DELIBERATELY BROKEN SYMMETRY

The two-lobed structure of the laser-induced breakdown plasma is highly symmetrical with respect to the focal plane. As a result, the gas flows approaching the plasma from opposite sides are approximately equal in strength. This generates a highly symmetrical toroidal plasma structure.

To show that this structure is a consequence of the symmetrical replenishment of the low-density region, the symmetry in the focal plane was deliberately broken by placing a metal plate 6.0 mm from the laser focus. The laser pulses pass through this metal plate through a 2.8 mm hole, large enough to allow them to pass freely.

The cross-sectional images presented in Fig. 15 show the development of a distorted toroidal structure as a result of the broken symmetry. Two white rectangles represent the metal plate to scale. The symmetry axis is represented by the horizontal dashed line, whereas the vertical dashed line is identical to the symmetry plane of the unmodified symmetrical experiment. Both dashed lines cross at the laser focus.

It is evident that the plasma pillbox is pushed aside as a result of the gas flow emanating from the hole in the metal plate. The same gas flow subsequently pierces through the center of the plasma pillbox, thereby again generating a toroidal structure.

Clearly, the metal plate is responsible for the distorted toroidal structure. Initially, the low-density region is rapidly expanding. The expansion along the symmetry axis is, of course, hindered by the metal plate. This limits the extent of the low-density region. The replenishing gas flow from beyond the metal plate, flowing through the small 2.8 mm hole, therefore commences in advance with respect to the flow generated by the collapse of the low-density region.

These flows therefore collide, not in the center of the toroidal plasma, but farther away from the metal plate. So they spread out, not in the symmetry plane of the unmodified symmetrical experiment, but into a cone at a distance to that plane. Because the flow generated by the collapse of the low-density region has a larger extent than the flow emanating from the small hole, a cone is the shape to be expected.

The colliding flows are difficult to distinguish at first, but come into sight as a distinct notch in the cross-sectional images at 24 μs. This notch corresponds to the horseshoe-shaped structure in the unmodified symmetrical experiment.

A closer examination of the cross-sectional images reveals that the plasma shows a revolving motion. This motion is a testimony of the presence of vorticity. Numerical studies on the fluid dynamical effects of laser energy deposition have shown that the generation of vorticity in these systems stems from the asymmetry of the breakdown plasma [40,65]. In this case the origin lies in the asymmetric experimental setting.

X. CONCLUSION

This paper demonstrates that the mechanism of Mach reflection is crucial in the formation of laser-generated, transient toroidal helium plasma at atmospheric pressure. A detailed experimental study, including Schlieren imaging, a novel plasma scanning-probe imaging technique, and tomographically reconstructed cross-sectional images, confirms the Mach reflection resulting from the two-lobed, laser-induced plasma kernel. Several complementary experiments were carried out to visualize the resulting formation of a toroidal plasma.

With this detailed understanding, a plasma reactor is currently being designed that will generate and sustain a compact toroidal plasma in free space, with potential applications in chemical reactors, plasma medicine, laser ignition of internal combustion engines, and linked magnetic field line plasma confinement.

ACKNOWLEDGMENTS

The authors are grateful to P. J. Bruggeman for stimulating discussions and for bringing reference [67] to our attention. They are furthermore grateful to C. B. Smiet for stimulating discussions and experimental support during the initial phase of this research and thank F. M. A. Smits for useful discussions and technical assistance with the experiment of Sec. IX. They also thank T. Blom, T. Boudewijn, V. M. Ramalho, and N. M. A. Scheinowitz for experimental support. Furthermore, D.B. is grateful to P. J. Bruggeman, R. Burgwal, D. Doelman, C. B. Smiet, J. Swearngin, A. Thompson, and S. Zwaan for stimulating discussions and support during the development of preliminary experimental setups. This work was supported by the NWO Spinoza Prize 2014 awarded to D.B. by the Dutch Research Council (NWO).

[1] C. Seward, Ball lightning events explained as self-stable spinning high-density plasma toroids or atmospheric spheromaks, IEEE Access **2**, 153 (2014).

[2] M. Gharib, S. Mendoza, M. Rosenfeld, M. Beizai, and F. J. A. Pereira, Toroidal plasmoid generation via extreme hydrodynamic shear, Proc. Natl. Acad. Sci. USA **114**, 12657 (2017).

[3] S. Stepanyan, N. Minesi, A. Tibère-Inglesse, A. Salmon, G. D. Stancu, and C. O. Laux, Spatial evolution of the plasma kernel produced by nanosecond discharges in air, J. Phys. D **52**, 295203 (2019).

[4] C. Dumitrache, R. VanOsdol, C. M. Limbach, and A. P. Yalin, Control of early flame kernel growth by multi-wavelength laser pulses for enhanced ignition, Sci. Rep. **7**, 10239 (2017).

[5] D. Bradley, C. G. W. Sheppard, I. M. Suardjaja, and R. Woolley, Fundamentals of high-energy spark ignition with lasers, Combust. Flame **138**, 55 (2004).

[6] M. S. Bak, S. Im, and M. A. Cappelli, Successive laser-induced breakdowns in atmospheric pressure air and premixed ethane-air mixtures, Combust. Flame **161**, 1744 (2014).

[7] J. Tauer, H. Kofler, K. Iskra, G. Tartar, and E. Wintner, Laser plasma-initiated ignition of engines, in *Proceedings of the 3rd International Conference on the Frontiers of Plasma Physics and Technology* (International Atomic Energy Agency, Bangkok, Thailand, 2007), p. S6.3, https://www-pub.iaea.org/MTCD/Publications/PDF/P_1357_CD_web/datasets/s6-3.html.

[8] M. Weinrotter, H. Kopecek, J. Graf, J. Klausner, G. Herdin, and E. Wintner, Laser ignition in internal combustion engines—A novel approach based on advanced lasers, Adv. Solid-State Photon. **98**, 812 (2005).

[9] D. Nassif and L. Hüwel, Appearance of toroidal structure in dissipating laser-generated sparks, J. Appl. Phys. **87**, 2127 (2000).

[10] S. S. Harilal, B. E. Brumfield, and M. C. Phillips, Lifecycle of laser-produced air sparks, Phys. Plasmas **22**, 063301 (2015).

[11] M. S. Bak, L. Wermer, and S. Im, Schlieren imaging investigation of successive laser-induced breakdowns in atmospheric-pressure air, J. Phys. D **48**, 485203 (2015).

[12] A. Bogaerts and E. C. Neyts, Plasma technology: An emerging technology for energy storage, ACS Energy Lett. **3**, 1013 (2018).

[13] K. H. Tsui, Magnetohydrodynamic model of equatorial plasma torus in planetary nebulae, Astron. Astrophys. **482**, 793 (2008).

[14] M. Laroussi, Cold plasma in medicine and healthcare: The new frontier in low temperature plasma applications, Front. Phys. **8**, 74 (2020).

[15] J. F. de la Fuente, A. A. Kiss, M. T. Radoiu, and G. D. Stefanidis, Microwave plasma emerging technologies for chemical processes, J. Chem. Tech. Biotech. **92**, 2495 (2017).

[16] G. Centi, G. Iaquaniello, and S. Perathoner, Chemical engineering role in the use of renewable energy and alternative carbon sources in chemical production, BMC Chem. Eng. **1**, 5 (2019).

[17] C. B. Smiet, S. Candelaresi, A. Thompson, J. Swearngin, J. W. Dalhuisen, and D. Bouwmeester, Self-organizing knotted magnetic structures in plasma, Phys. Rev. Lett. **115**, 095001 (2015).

[18] H. K. Moffatt, The degree of knottedness of tangled vortex lines, J. Fluid Mech. **35**, 117 (1969).

[19] A. M. Kamchatnov, Topological solitons in magnetohydrodynamics, Sov. Phys. J. Exp. Theor. Phys. **55**, 69 (1982).

[20] A. Thompson, J. Swearngin, A. Wickes, and D. Bouwmeester, Constructing a class of topological solitons in magnetohydrodynamics, Phys. Rev. E **89**, 043104 (2014).

[21] A. F. Rañada, A topological theory of the electromagnetic field, Lett. Math. Phys. **18**, 97 (1989).

[22] W. T. M. Irvine and D. Bouwmeester, Linked and knotted beams of light, Nat. Phys. **4**, 716 (2008).

[23] H. Kedia, I. Bialynicki-Birula, D. Peralta-Salas, and W. T. M. Irvine, Tying knots in light fields, Phys. Rev. Lett. **111**, 150404 (2013).

[24] A. J. J. M. de Klerk, R. I. van der Veen, J. W. Dalhuisen, and D. Bouwmeester, Knotted optical vortices in exact solutions to Maxwell's equations, Phys. Rev. A **95**, 053820 (2017).

[25] A. Thompson, J. Swearngin, and D. Bouwmeester, Linked and knotted gravitational radiation, J. Phys. A: Math. Theor. **47**, 355205 (2014).

[26] C. B. Smiet, H. J. de Blank, T. A. de Jong, D. N. L. Kok, and D. Bouwmeester, Resistive evolution of toroidal field distributions and their relation to magnetic clouds, J. Plasma Phys. **85**, 905850107 (2019).

[27] G. B. Rybicki and A. P. Lightman, *Radiative Processes in Astrophysics* (John Wiley & Sons, New York, 1979).

[28] J. Cooper, Plasma spectroscopy, Rep. Prog. Phys. **29**, 35 (1966).

[29] I. H. Hutchinson, *Principles of Plasma Diagnostics*, 2nd ed. (Cambridge University Press, Cambridge, 2002).

[30] M. Smerlak, A blackbody is not a blackbox, Eur. J. Phys. **32**, 1143 (2011).

[31] C. G. Schregel, E. A. D. Carbone, D. Luggenholscher, and U. Czarnetzki, Ignition and afterglow dynamics of a high pressure nanosecond pulsed helium micro-discharge: I. Electron, Rydberg molecules and He (2^3S) densities, Plasma Sources Sci. Technol. **25**, 054003 (2016).

[32] E. A. D. Carbone, C. G. Schregel, and U. Czarnetzki, Ignition and afterglow dynamics of a high pressure nanosecond pulsed helium micro-discharge: II. Rydberg molecules kinetics, Plasma Sources Sci. Technol. **25**, 054004 (2016).

[33] A. Kramida, Y. Ralchenko, J. Reader, and NIST ASD Team, NIST Atomic Spectra Database, National Institute of Standards and Technology (2019).

[34] T. C. Williams and C. R. Shaddix, Simultaneous correction of flat field and nonlinearity response of intensified charge-coupled devices, Rev. Sci. Instrum. **78**, 123702 (2007).

[35] W. G. Wagner and B. A. Lengyel, Evolution of the giant pulse in a laser, J. Appl. Phys. **34**, 2040 (1963).

[36] Y. P. Raizer, *Gas Discharge Physics* (Springer-Verlag, Berlin, 1991).

[37] A. W. Miziolek, V. Palleschi, and I. Schechter, *Laser Induced Breakdown Spectroscopy* (Cambridge University Press, Cambridge, 2006).

[38] A. Alberti, A. Munafò, C. Pantano, J. B. Freund, and M. Panesi, Modelling of air breakdown by single-mode and multi-mode lasers, AIAA Scitech 2019 Forum 1 (2019).

[39] Y. Chen, J. W. L. Lewis, and C. Parigger, Spatial and temporal profiles of pulsed laser-induced air plasma emissions, J. Quant. Spectrosc. Radiat. Transfer **67**, 91 (2000).

[40] S. Ghosh and K. Mahesh, Numerical simulation of the fluid dynamic effects of laser energy deposition in air, J. Fluid Mech. **605**, 329 (2008).

[41] A. Alberti, A. Munafò, M. Koll, M. Nishihara, C. Pantano, J. B. Freund, G. S. Elliott, and M. Panesi, Laser-induced non-equilibrium plasma kernel dynamics, J. Phys. D **53**, 025201 (2020).

[42] A. Alberti, A. Munafò, C. Pantano, J. B. Freund, and M. Panesi, Radiation supported plasma waves in non-equilibrium laser discharges, in *8th International Workshop on Radiation of High Temperature Gases for Space Missions* (2019).

[43] M. Nishihara, J. B. Freund, N. G. Glumac, and G. S. Elliott, Influence of mode-beating pulse on laser-induced plasma, J. Phys. D **51**, 135601 (2018).

[44] G. S. Settles, *Schlieren and Shadowgraph Techniques* (Springer-Verlag, Berlin, 2001).

[45] M. I. Suresh, F. Köttig, J. R. Koehler, F. Tani, and P. S. Russell, Pump-probe study of plasma dynamics in gas-filled photonic crystal fiber using counterpropagating solitons, Phys. Rev. Appl. **12**, 064015 (2019).

[46] C. Gautier, P. Fichet, D. Menut, J.-L. Lacour, D. L'Hermite, and J. Dubessy, Study of the double-pulse setup with an orthogonal beam geometry for laser-induced breakdown spectroscopy, Spectrochim. Acta, Part B **59**, 975 (2004).

[47] G. I. Taylor, The formation of a blast wave by a very intense explosion. I. Theoretical discussion, Proc. R. Soc. London A **201**, 159 (1950).

[48] G. I. Taylor, The formation of a blast wave by a very intense explosion. II. The atomic explosion of 1945, Proc. R. Soc. London A **201**, 175 (1950).

[49] H. A. Bethe, K. Fuchs, J. O. Hirschfelder, J. L. Magee, R. E. Peierls, and J. Von Neumann, *Blast Wave* (Los Alamos Scientific Laboratory New Mexico, 1958).

[50] D. F. Cioffi, Supernova remnants as probes of the interstellar medium, in *Physical Processes in Hot Cosmic Plasmas*, NATO ASI Series Vol. 305 (Springer, Dordrecht, 1990).

[51] F. H. Shu, *The Physics of Astrophysics: Gas Dynamics* (University Science Books, Mill Valley, CA, 1992).

[52] L. I. Sedov, *Similarity and Dimensional Methods in Mechanics* (Academic Press, New York, 1959).

[53] Y. B. Zel'dovich and Y. P. Raizer, *Physics of Shock Waves and High-Temperature Hydrodynamic Phenomena* (Academic Press, New York, 1966).

[54] G. Cristoforetti, S. Legnaioli, L. Pardini, V. Palleschi, A. Salvetti, and E. Tognoni, Spectroscopic and shadowgraphic analysis of laser induced plasmas in the orthogonal double pulse pre-ablation configuration, Spectrochim. Acta Part B **61**, 340 (2006).

[55] P. Krehl and M. Van der Geest, The discovery of the Mach reflection effect and its demonstration in an auditorium, Shock Waves **1**, 3 (1991).

[56] S. Glasstone and P. J. Dolan, *The Effects of Nuclear Weapons*, 3rd ed. (Department of Defense, Washington, DC, 1977).

[57] E. Mach and L. Mach, Ueber die Interferenz der Schallwellen von grosser Excursion, Ann. Phys. **277**, 140 (1890).

[58] P. Krehl, Shock wave physics and detonation physics—A stimulus for the emergence of numerous new branches in science and engineering, Eur. Phys. J. H **36**, 85 (2011).

[59] H. R. Griem, *Principles of Plasma Spectroscopy* (Cambridge University Press, Cambridge, 1997).

[60] V. Dribinski, A. Ossadtchi, V. A. Mandelshtam, and H. Reisler, Reconstruction of Abel-transformable images: The Gaussian basis-set expansion Abel transform method, Rev. Sci. Instrum. **73**, 2634 (2002).

[61] R. N. Bracewell, Strip integration in radio astronomy, Aust. J. Phys. **9**, 198 (1956).

[62] K. M. Hanson, Special topics in test methodology: Tomographic reconstruction of axially symmetric objects from a single dynamic radiograph, Prog. Astronaut. Aeronaut. **155**, 687 (1993).

[63] G. Pretzier, H. Jäger, T. Neger, H. Philipp, and J. Woisetschläger, Comparison of different methods of Abel inversion using computer simulated and experimental side-on data, Z. Naturforsch. A **47**, 955 (1992).

[64] D. G. Akhmetov, *Vortex Rings* (Springer-Verlag, Berlin, 2009).

[65] M. H. Morsy and S. H. Chung, Numerical simulation of front lobe formation in laser-induced spark ignition of CH_4/air mixtures, Proc. Combust. Inst. **29**, 1613 (2002).

[66] J. H. Jeans, *An Introduction to the Kinetic Theory of Gases* (Cambridge University Press, Cambridge, 1940).

[67] E. Nedanovska, G. Nersisyan, T. J. Morgan, L. Huwel, T. Murakami, C. L. S. Lewis, D. Riley, and W. G. Graham, Investigating the dynamics of laser induced sparks in atmospheric helium using Rayleigh and Thomson scattering, J. Appl. Phys. **117**, 013302 (2015).

[68] L. M. Chanin, A. V. Phelps, and M. A. Biondi, Measurements of the attachment of low-energy electrons to oxygen molecules, Phys. Rev. **128**, 219 (1962).

[69] W. M. Haynes, *CRC Handbook of Chemistry and Physics*, 95th ed. (CRC Press, Boca Raton, FL, 2014).

[70] W. H. Besant, *A Treatise on Hydrostatics and Hydrodynamics* (Deighton, Bell, and Co., Cambridge, 1859).

[71] Lord Rayleigh, On the pressure developed in a liquid during the collapse of a spherical cavity, London Edinburgh Dublin Philos. Mag. J. Sci. **34**, 94 (1917).

[72] G. Sinibaldi, A. Occhicone, F. Alves Pereira, D. Caprini, L. Marino, F. Michelotti, and C. M. Casciola, Laser induced cavitation: Plasma generation and breakdown shockwave, Phys. Fluids **31**, 103302 (2019).

[73] L. D. Landau and E. M. Lifshitz, *Fluid Mechanics*, 2nd ed. (Pergamon Press, Oxford, 1987).